Seasonality and Variability of Snowfall to Total Precipitation Ratio over High Mountain Asia Simulated by the GFDL High-Resolution AM4

WENHAO DONG[a,b] AND YI MING[a]

[a] *NOAA/Geophysical Fluid Dynamics Laboratory, Princeton, New Jersey*
[b] *Cooperative Programs for the Advancement of Earth System Science, University Corporation for Atmospheric Research, Boulder, Colorado*

ABSTRACT: The ratio of snowfall to total precipitation (S/P ratio) is an important metric that is widely used to detect and monitor hydrologic responses to climate change over mountainous areas. Changes in the S/P ratio over time have proved to be reliable indicators of climatic warming. In this study, the seasonality and interannual variability of monthly S/P ratios over High Mountain Asia (HMA) have been examined during the period 1950–2014 based on a three-member ensemble of simulations using the latest GFDL AM4 model. The results show a significant decreasing trend in S/P ratios during the analysis period, which has mainly resulted from reductions in snowfall, with increases in total precipitation playing a secondary role. Significant regime shifts in S/P ratios are detected around the mid-1990s, with rainfall becoming the dominant form of precipitation over HMA after the changepoints. Attribution analysis demonstrates that increases in rainfall during recent decades were primarily caused by a transformation of snowfall to rainfall as temperature warmed. A logistic equation is used to explore the relationship between the S/P ratio and surface temperature, allowing calculation of a threshold temperature at which the S/P ratio equals 50% (i.e., precipitation is equally likely to take the form of rainfall or snowfall). These temperature thresholds are higher over higher elevations. This study provides an extensive evaluation of simulated S/P ratios over the HMA that helps clarify the seasonality and interannual variability of this metric over the past several decades. The results have important socioeconomic and environmental implications, particularly with respect to water management in Asia under climate change.

KEYWORDS: Atmosphere; Precipitation; Snowfall; Climate models; Interannual variability; Seasonal variability

1. Introduction

High Mountain Asia (HMA) is an elevated geographic region extending from the Himalayas in the south and east to the Hindu Kush in the west and the Tien Shan in the north (Fig. 1). It includes many of the most prominent Asian mountain ranges stretching across the Tibetan Plateau. These towering peaks are home to a great diversity of wildlife and a unique high-altitude ecosystem. Moreover, these mountains hold the world's largest reservoir of perennial glaciers and snow outside of the polar regions, and act as an important buffer in the hydrological system (Xu et al. 2008; Yao et al. 2012; Yang et al. 2014; IPCC 2019). Over one-sixth of the global population lives downstream of these reservoirs. Their livelihood depends heavily on rivers with headwaters in HMA, which provide water for irrigation, hydropower, and many other purposes. However, rapid population growth and industrialization in the surrounding nations, in tandem with climate change, are exerting increased pressure on water resources in this region.

Precipitation is the ultimate source of water supplies in these mountainous areas. Replenishment via precipitation has great impacts on glacier mass balance, river discharge, plant phenology, and natural hazards (Yao et al. 2012; Lutz et al. 2014; Maussion et al. 2014; Mölg et al. 2014). Numerous studies have analyzed variations of precipitation amounts over HMA. An overall wetting trend has been reported over the Tibetan Plateau during the past several decades, but with substantial regional and seasonal disparities (Yang et al. 2011; Maussion et al. 2014; Wang et al. 2018). Significant decreasing trends in summer rainfall over the southwestern Tibetan Plateau have been noted during the second half of the last century (Dong et al. 2016), which are linked to changes in the occurrence and characteristics of low pressure systems over the Indian subcontinent (Dong et al. 2017, 2020). Similarly, Wang and Yin (2019) found a significant drying trend over the arid and semiarid regions of the Tibetan Plateau during 1990–2014 based on a self-organizing map analysis. Over the Qilian Mountains, no significant trends were detected in annual precipitation during 1961–2010 (Tian et al. 2014); however, warm season rainfall over the Tien Shan mountain range has decreased in contrast to that over the adjacent basin regions during the past two decades (Dong et al. 2018a). In addition to the amount of precipitation, which is the main determinant of variations in total available water resources, the phase of precipitation (i.e., snowfall vs rainfall) could also play a critical role in modulating
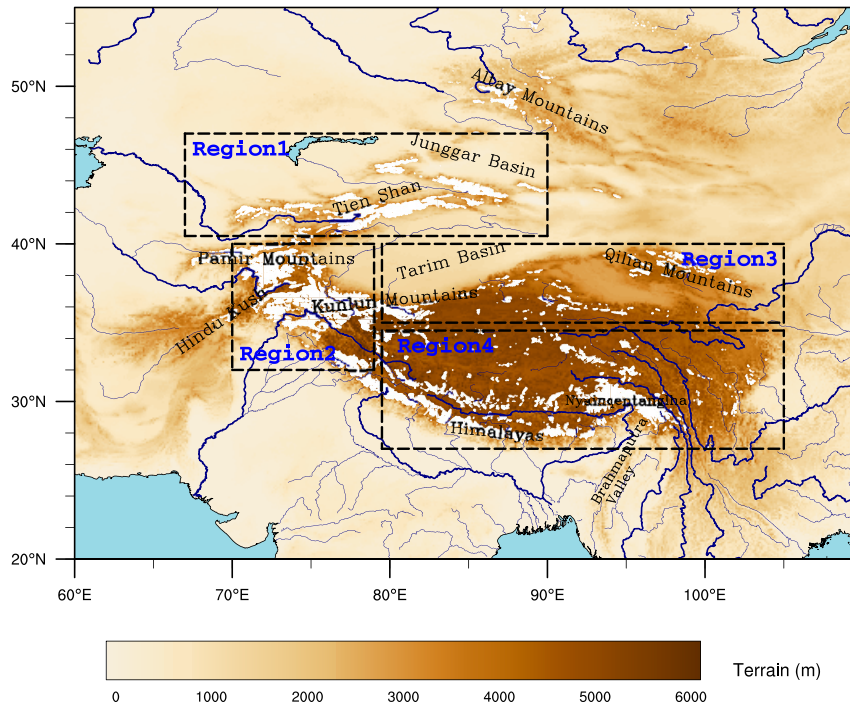
Fig. 1. Topography in the High Mountain Asia (HMA) region based on the ETOPO1 global relief model. Topography used in C192AM4 is shown in Fig. S1 in the online supplemental material. Glaciers over HMA are drawn in white based on the GLIMS Glacier Database (Raup et al. 2007) provided by the National Snow and Ice Data Center. Major rivers are drawn in thicker blue lines with tributaries in thinner blue lines. Geographical locations mentioned in the text are indicated. Four regions of interest are bounded by the black dashed rectangles: the Tien Shan (region 1), the Karakoram (region 2), the northern Tibetan Plateau (region 3), and the southern Tibetan Plateau (region 4).

climate in mountainous regions (Guo and Li 2015; Deng et al. 2017; Zhu et al. 2017; Jennings et al. 2018). Snowfall and rainfall have distinct effects on land surface water and energy fluxes. Snowfall stores a portion of the wintertime precipitation into the summer months, helping to buffer the hydrological system, while rainfall infiltrates soils relatively quickly before converging into nearby rivers or groundwater. The presence of snow also increases the surface albedo, resulting in regional cooling over snow-covered regions. By contrast, albedo often decreases when precipitation occurs in the form of rainfall as wet lands are usually darker and have a lower albedo (Levine and Boos 2017).

The hydrologic cycle is expected to intensify over HMA as climate warms (Yang et al. 2011, 2014). More intense rainfall and earlier snowfall events have been observed over this region (Dong et al. 2018b; Ding et al. 2019). Moreover, warm temperatures have reduced the proportional amount of snowfall versus rainfall worldwide, a trend that is expected to accelerate over the next several decades (Knowles et al. 2006; Wang et al. 2016; Jennings et al. 2018). In this context, both the amount and phase of precipitation are likely to change as climate continues to warm. These changes have socioeconomic and environmental consequences at scales ranging from local to continental, reducing the length of the snowy season and

resulting in earlier snowmelt. As a result, glaciers are melting, snow cover and permafrost are disappearing, and water availability is changing in a chain of events over HMA, placing local and downstream communities and ecosystems at progressively greater risks of both short-term flooding and long-term water shortages. Much of the work assessing changes in precipitation over mountainous areas has focused on the ratio of snowfall to total precipitation (S/P), a hydrologic indicator that is sensitive to climate variability and widely used to detect and monitor hydrologic responses to climate change (Huntington et al. 2004; Knowles et al. 2006; Feng and Hu 2007). Changes in S/P ratios over time could influence the magnitude and timing of spring runoff and its contributions to the summer base flow (Huntington et al. 2004; Knowles et al. 2006; Feng and Hu 2007).

Increases in temperature and decreases in snowfall have been observed in many studies focusing on HMA (Immerzeel et al. 2015; Bibi et al. 2018). These changes could modify the S/P ratio dramatically. A detailed spatial assessment of changes in S/P ratios within this region is thus urgently needed. A few studies have assessed changes in these regions over different patches of HMA, mainly using station records. Based on daily precipitation and temperature records, Wang et al. (2016) reported a decreasing trend in the S/P ratio over the eastern Tibetan Plateau. A similar conclusion was drawn by

Zhu et al. (2017), who investigated S/P ratios over permafrost and seasonal frozen ground regions of the plateau using station records. A downward trend in S/P ratios during the cold season has also been identified over the Tien Shan during 1961–2010 (Guo and Li 2015). Li et al. (2018) revealed opposing trends in S/P ratios over low-elevation and high-elevation regions of northwestern China during 1979–2015 based on regional model simulations. Such a disparity was attributed to different changes in snowfall and precipitation as climate warms. However, most of these studies are confined to the limited numbers and sampling domains of meteorological stations in these regions, and several aspects of the results remain controversial. This lack of consensus is aggravated by a lack of observational data with sufficient spatial and temporal coverage. While this is due to a general lack of data recording precipitation phase, studies based on remotely sensed data usually have used the temperature threshold or other temperature-related methods to estimate snowfall assuming its occurrence probability (Wang et al. 2016; Deng et al. 2017; Li et al. 2018). However, Jennings et al. (2018) found significant spatial variations in rain–snow temperature thresholds over HMA. These variations may partially explain the lack of a spatially uniform response to climate forcing within the HMA cryosphere (Yao et al. 2012; Kapnick et al. 2014; Mölg et al. 2014).

Here, we approach this problem using a combination of station-based observations, regional model outputs, and a unique multimember ensemble of GCM simulations performed at NOAA GFDL. Application of atmospheric models with parameterized microphysics schemes has been shown to be a more reliable option for predicting the phase of precipitation than temperature threshold methods (Ikeda et al. 2010; Harpold et al. 2017; Jennings et al. 2018). GFDL models have previously been used to study the hydroclimate over HMA. Kapnick et al. (2014) used the GFDL CM2.5 model (Delworth et al. 2012) to investigate the sensitivity of snowfall to warming over the Karakoram range, and showed that the model simulated the hydroclimate of this region well. Based on these model simulations, they found that local meteorological conditions are important factors behind regional differences in how glaciers respond to climate warming. In this study, we use high-resolution simulations (~50 km) from the latest GFDL AM4 model (Zhao et al. 2018a,b). We focus on elucidating how the S/P ratio has changed over the HMA during the past 65 years (1950–2014). The data, methods, and model are introduced in section 2. The results are described in section 3. Extensive validation of the model simulation is conducted in sections 3a and 3b via comparisons with observations and regional model outputs. A detailed analysis of the S/P ratio, including trend and regime shift analyses in different seasons and at different elevations, is then presented in section 3c. The individual contributions of changes in snowfall and total precipitation to changes in the S/P ratios are evaluated in section 3d, followed by a logistic analysis of the relationship between the S/P ratio and surface temperature in section 3e. An attribution analysis of the contributions of local temperature relative to large-scale circulation to changes in rainfall

is presented and discussed in section 3f. The conclusions are given in section 4.

2. Data and method

a. Gridded observational data

The Asian Precipitation–Highly Resolved Observational Data Integration Toward Evaluation of Water Resources (APHRODITE) project monthly total precipitation and surface temperature products at 0.25° resolution are used as observational benchmarks in this study. This product uses most of the available rain gauge observation network across Asia, and is the only long-term continental-scale product containing a dense network of daily gauge-based data for Asia that includes most of the high-altitude areas. For regions with sparse observational stations, it employs a Sheremap-type scheme using angular distance weights for interpolation (Yatagai et al. 2012). This interpolation method has been shown to yield better representation of orographic features. The latest version of APHRODITE products covering the period 1998–2014 is adopted in this study (V1808 for surface temperature and V1801R1 for precipitation). These products have been improved from previous versions, especially with regard to the representation of extreme precipitation events. More details about APHRODITE data products are available at www.chikyu.ac.jp/precip.

Regional climate model experiments, although typically limited in duration due to the computational expense involved, have been used to reproduce regional hydroclimate in many regions around the world. The High Asia Refined analysis (HAR), generated using a configuration of the WRF model following a dynamical downscaling method and a daily reinitialization strategy [see Maussion et al. (2014) for details], is used as an alternative reference for model validation in this study. HAR products are provided for the period 2000–14 for two different spatial domains at two different resolutions. We use the relatively coarse 30-km gridded dataset, which includes most mountain ranges in southern and central Asia. The HAR precipitation (both rainfall and snowfall) and temperature datasets have been widely used and validated against available station and in situ campaign measurements in a variety of studies focusing on hydroclimate within HMA. Results have shown that the HAR dataset is able to reproduce both liquid and frozen precipitation well (Mölg and Scherer 2012; Maussion et al. 2014; Mölg et al. 2014; Dong et al. 2016, 2018b).

b. Description of the GFDL C192AM4 model

We use outputs from the latest atmospheric GCM developed by GFDL, AM4. The AM4 model serves as the atmospheric component for the CMIP6-era GFDL coupled climate and Earth system models (Zhao et al. 2018a,b; Held et al. 2019; Dunne et al. 2020). As with the default AM4, these high-resolution simulations [referred to as C192AM4; see details in Zhao (2020)] are performed with a few tuning strategies. C192 here denotes the cubed-sphere topology with 192 × 192 grid boxes per cube face, which yields a

grid spacing of approximately 50 km. The model grid has 33 vertical levels with more emphasis on troposphere compared to the stratosphere. The model top is located at 1 hPa. For the AMIP-mode simulations examined in this work, the model is driven by time-varying boundary conditions, as well as natural and anthropogenic forcings developed for CMIP6 experiments (Eyring et al. 2016; archived at https://esgf-node.llnl.gov/projects/input4mips/). The performance of the model in simulating the spatial distribution of meteorological fields such as winds, temperature, humidity, clouds, atmospheric tracers, and energy fluxes in AMIP mode has already been assessed in great detail via comparisons with both CMIP5 AMIP simulations and past GFDL model simulations (Zhao et al. 2018a,b). The new version of the model adopted here performs well overall in comparison with previous GFDL models (Zhao 2020). The comparison with the CMIP5 model is also favorable, indicating improvements even relative to the best-performing CMIP5 models (Zhao et al. 2018a). It has also been used to assess various important weather phenomena associated with precipitation, such as atmospheric rivers, tropical storms, and mesoscale convective systems (Dong et al. 2021; Zhao 2020, 2022). It is found that the mean distribution of the atmospheric river and mesoscale convective systems as well as the associate precipitation are reasonably simulated by this model over HMA. Monthly mean outputs covering the period of 1950–2014, including surface temperature, total precipitation, snowfall, and rainfall, taken from a three-member ensemble generated using slightly different initial conditions, are used in this study.

c. Selection of study area

Interannual variability in S/P ratios is assessed both for different seasons and for different elevations. To account for the geographic complexity of the HMA region, we separate it into four subregions (black dashed rectangles in Fig. 1): region 1, the Tien Shan mountain ranges; region 2, the Karakoram region as defined by Kapnick et al. (2014); region 3, the northern Tibetan Plateau; and region 4, the southern Tibetan Plateau. These regions are selected due to their distinctive features as reported in previous work. For example, hydroclimatic changes over the Tien Shan mountain ranges are distinct from those in surrounding regions (Dong et al. 2018a), while region 2 features the so-called Karakoram anomaly, in which glacier mass has increased during recent decades even as most glaciers within HMA have melted under widespread warming. The Karakoram anomaly has been attributed to both unique regional atmospheric circulation variability (Forsythe et al. 2017) and local meteorological forcing (Kapnick et al. 2014). Regions 3 and 4 are separated by the parallel at 35°N, which approximates the natural boundary between the two dominant large-scale circulation regimes in this region, namely the midlatitude westerly jet and the Asian monsoon (Tian et al. 2001; Yao et al. 2012; Dong et al. 2017).

d. Statistical analysis

Trends in the S/P ratio and other meteorological factors are calculated using the robust Theil–Sen estimator (Theil 1950;

Sen 1968). This method is designed to reduce the effects of outliers and end points in linear trend analysis. A regime-shift detection method, namely the changepoint analysis, is applied to probe the possibility of abrupt changes in the variables (Chen and Gupta 2012). This method has been widely used to detect abrupt shifts in climate time series (e.g., mean, variance, or trend). It calculates the timing and number of changepoints in a time series. Differences are evaluated using the two-tailed Student's t test. Climate shifts and differences are reported only if they are found to be statistically significant at the 95% confidence level.

e. S/P ratio trend analysis

We compare the respective contributions of trends in rainfall and snowfall to trends in S/P ratios. By definition, an S/P ratio trend can be written as

$$\left(\frac{S}{P}\right)' = \frac{S'P - SP'}{P^2}, \tag{1}$$

where S and P denote snowfall and total precipitation, respectively, and the prime indicates the trend based on the Theil–Sen estimator. Via algebraic manipulation of Eq. (1), we have

$$\left(\frac{S}{P}\right)' = \frac{S}{P}[(\ln S)' - (\ln P)'], \tag{2}$$

where $\ln S$ and $\ln P$ indicate the logarithms of snowfall and total precipitation, respectively. The sign of the S/P ratio trend is thus determined by the relative magnitudes of trends in the logarithms of snowfall and total precipitation rather than the trends in snowfall and precipitation directly.

f. Regression analysis between the S/P ratio and surface temperature

Although other parameters matter (such as relative humidity and surface wind), whether falling precipitation takes the solid or liquid form depends in large part on the surface air temperature (Legates and Bogart 2009; Deng et al. 2017). This relationship serves as the rationale for using surface air temperature to distinguish different precipitation types, as applied in many studies. Various relationships between the S/P ratio and surface air temperature have been proposed. Among these, the logistic curve has been shown to yield the best fit to observational data (Førland and Hanssen-Bauer 2000; Legates and Bogart 2009; Krasting et al. 2013). This fit follows the form

$$f(\overline{T}_a) = \frac{1}{1 + a\,b^{\overline{T}_a}}, \tag{3}$$

where $f(\overline{T}_a)$ is the S/P ratio at a surface air temperature of $\overline{T}_a$ (units: °C) and the parameters a and b are fitting constants. The slope of this relationship is always negative, indicating that increases in temperatures lead to lower values of $f(\overline{T}_a)$ or, equivalently, an increased fraction of total precipitation falling in liquid form as climate warms. Mean values of $a = 1.61$ and $b = 1.35$ have been empirically derived to fit monthly mean S/P ratios to observed surface air temperatures based on

various datasets sampled in the Northern Hemisphere (Rawlins et al. 2006; Krasting et al. 2013; Bintanja 2018). In this study, we use the logistic form to fit S/P ratios to surface air temperatures in HMA and derive the corresponding constants a and b for this region. Absolute mean errors are also reported for each fit.

g. Attribution analysis of the rainfall-dominant HMA

As indicated by Eq. (3), a warming climate will increase the fraction of total precipitation falling as rainfall. In other words, we expect precipitation in HMA to become increasingly dominated by rainfall as climate warms. However, increases in rainfall may arise either from temperature changes (i.e., the part of rainfall that is transformed from snowfall) or from changes in total precipitation (i.e., the part related to changes in the large-scale circulation). We therefore conduct an attribution analysis to probe the relative importance of changes in the large-scale circulation (related to total precipitation) and changes in local temperature (related to the transformation of snowfall to rainfall) to changes in rainfall amount. We select two periods that follow from the climate regime changepoint analysis. We then calculate the relative changes of snowfall, rainfall, and total precipitation during these two periods:

$$\begin{cases} \Delta P = P_1 - P_2 \\ \Delta S = S_1 - S_2 \\ \Delta R = R_1 - R_2 \end{cases}, \qquad (4)$$

where R is liquid precipitation (i.e., rainfall) and the subscripts 1 and 2 correspond to the two different periods. Substituting $f = S/P$ and $\Delta P = \Delta R + \Delta S$ into Eq. (4), we derive expressions for ΔS and ΔR in terms of changes in temperature and total precipitation:

$$\begin{cases} \Delta S = P_2 \Delta f + f_1 \Delta P \\ \Delta R = -P_2 \Delta f + (1 - f_1) \Delta P \end{cases}. \qquad (5)$$

This method has been applied in several previous studies (Krasting et al. 2013; Bintanja 2018). Here, we focus solely on changes in rainfall in the context of climatic warming over HMA. We therefore define $-P_2 \Delta f$ as the component of changes in rainfall that we attribute to temperature changes (i.e., the part of snowfall that is transformed into rainfall due to changes in temperature) and $(1 - f_1) \Delta P$ as the component related to changes in total precipitation.

3. Results

a. Mean HMA climate simulated by C192AM4

We start with an overall assessment of the climatological features over HMA from C192AM4 model simulations. Figures 2a–f show long-term means and linear trends of total precipitation, snowfall, and surface air temperature during the 1950–2014 study period. The model results presented throughout this study are based on the average of the three ensemble members unless otherwise stated. The total precipitation shows a southeast-to-northwest gradient across HMA, consistent with the distribution of moisture transport (Yao et al. 2012).

A center of enhanced precipitation linked to orographic uplift is found over the southern periphery of the Tibetan Plateau (Fig. 2a). By contrast, the distribution of snowfall shows large values mainly over higher elevations (Fig. 2b) and corresponds well to the locations of major glaciers shown in Fig. 1. When categorized into different elevation bins, the average total precipitation peaks in the 3500–4000-m altitude range while the average snowfall peaks in the higher 4000–4500-m altitude range (Figs. 2g,h). The long-term mean temperature distribution depends primarily on the underlying surface elevation, with an average lapse rate of about 3.46°C km^{-1} (Figs. 2c,i).

Linear trends in these variables are calculated using the Theil–Sen estimator applied to the entire 65-yr period. Replacing the ensemble mean with each member yields similar results. For total precipitation, positive trends are simulated over large parts of the central TP, with significant changes noted over the southeastern corner of the TP (Fig. 2d). This increasing trend has been linked to an intensification of moisture transport through the Brahmaputra Valley (Song et al. 2011). Meanwhile, significant decreases in total precipitation are simulated over the eastern periphery of the TP, in good agreement with station records in this area (Cuo et al. 2013; Zhang et al. 2019). We find a greater tendency toward positive precipitation trends at higher elevations (Fig. 2g). The spatial distribution of trends in snowfall (Fig. 2e) differs substantially from that for trends in total precipitation. Most parts of HMA show decreasing trends in snowfall, with only a few high-elevation regions (such as the Nyainqentanglha Range and the Karakoram region) showing insignificant increasing trends. We generally find stronger negative trends in snowfall at higher altitudes; however, this relationship is not monotonic, especially at the highest altitudes (Fig. 2h). The resulting "boomerang" shape in snowfall trends with altitude is in accordance with the results of Deng et al. (2017) based on station records. By contrast, warming in surface air temperatures is fairly uniform across HMA. Temperature trends indicate warming at a rate of about 0.15°C decade^{-1} ($P < 0.01$) when averaged over the whole of HMA, which is larger than the global average during this period (Yang et al. 2014; Ma et al. 2017). But the simulated warming rate is much smaller than that based on the station records, which shows an average rate of 0.3°C decade^{-1} with a likely range of ±0.2°C decade^{-1} (Wang et al. 2008; IPCC 2019). This may be subject to the coarse resolution of the model, which fails to fully resolve the distribution of temperature with sharp gradient over the complex terrain. An additional elevation-dependent warming (i.e., the enhancement of warming rates with elevation) of about 5% with respect to the mean warming rate per kilometer is simulated within HMA, which is again in good agreement with previous reports (Liu and Chen 2000; Yao et al. 2000; Pepin et al. 2015).

b. Comparisons with HAR and APHRODITE

As shown above, the mean climate simulated by the C192AM4 model is broadly consistent with previous studies
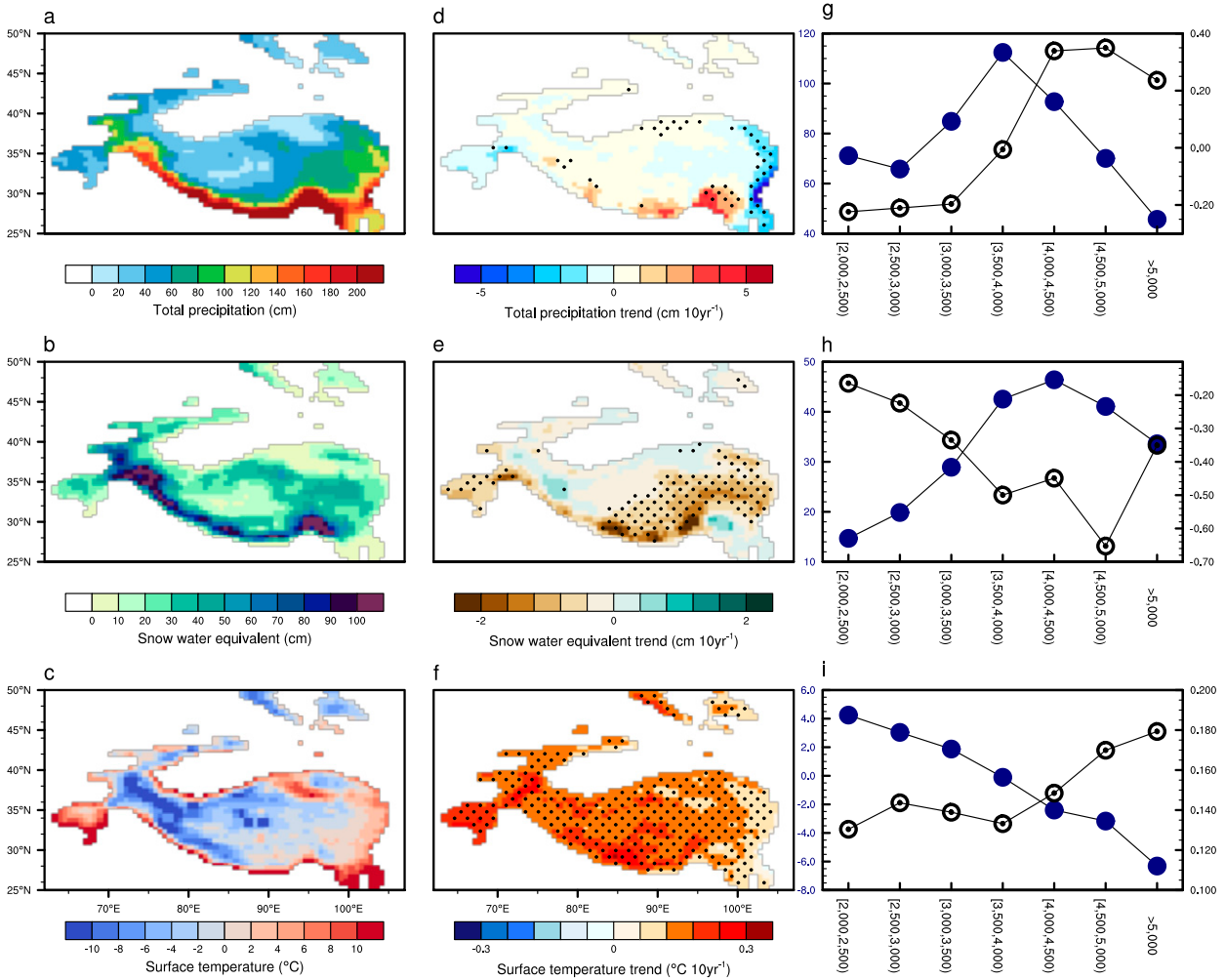
FIG. 2. C192AM4 simulated climate features over the High Mountain Asia. (left) Long-term means of simulated (a) total precipitation, (b) snow water equivalent, and (c) surface temperature averaged over 1950–2014. (center) Linear trends in (d) total precipitation, (e) snow water equivalent, and (f) surface temperature during 1950–2014. Dots in (d)–(f) indicate trends that are statistically significant at the 95% confidence level. (right) Long-term means (blue filled markers; left y axis) and linear trends (black bull's-eye markers; right y axis) of (g) total precipitation, (h) snow water equivalent, and (i) surface temperature binned by elevation into 500-m intervals from 2000 to 5000 m above mean sea level. Note the different y-axis scales in (g)–(i).

based mainly on station records. However, the relatively sparse coverage of station data within the HMA domain makes it difficult to provide a comprehensive description of the hydroclimate. Therefore, in this section, we further evaluate the C192AM4 simulation by comparing it with climatic data from HAR and APHRODITE.

The 3-month seasonal means of total precipitation, snowfall, and surface air temperature over the four subregions of HMA are shown in Fig. 3. The use of 3-month seasonal means instead of individual months is to facilitate a comparison with previous studies, which usually focus on one or more specific season(s). However, we should point out that the conclusions are not affected if the value from each month is present. For total precipitation, the C192AM4 simulations are in good agreement with the HAR dataset over the Karakoram and northern Tibetan Plateau regions, but they differ over the

southern Tibetan Plateau and the Tien Shan mountain ranges. The poor agreement in region 1 between C192AM4 and HAR may be associated with different seasonal cycles of precipitation over high and low elevations, given the geographic complexity of the Tien Shan region. As shown in Fig. S1 in the online supplemental material, the underlying orography in this subregion differs substantially between C192AM4 and HAR due to their different horizontal resolutions. The larger bias over the southern Tibetan Plateau in C192AM4, especially during summertime, might be linked to the influence of the Indian summer monsoon, which is found to be stronger in the model (Dong et al. 2020). Besides, the coarse resolution of the model also leads to excessive atmospheric water vapor transport into this region (Lin et al. 2018). GCMs often overestimate dynamical orographic precipitation, as documented in previous lower-resolution CMIP5 modeling work
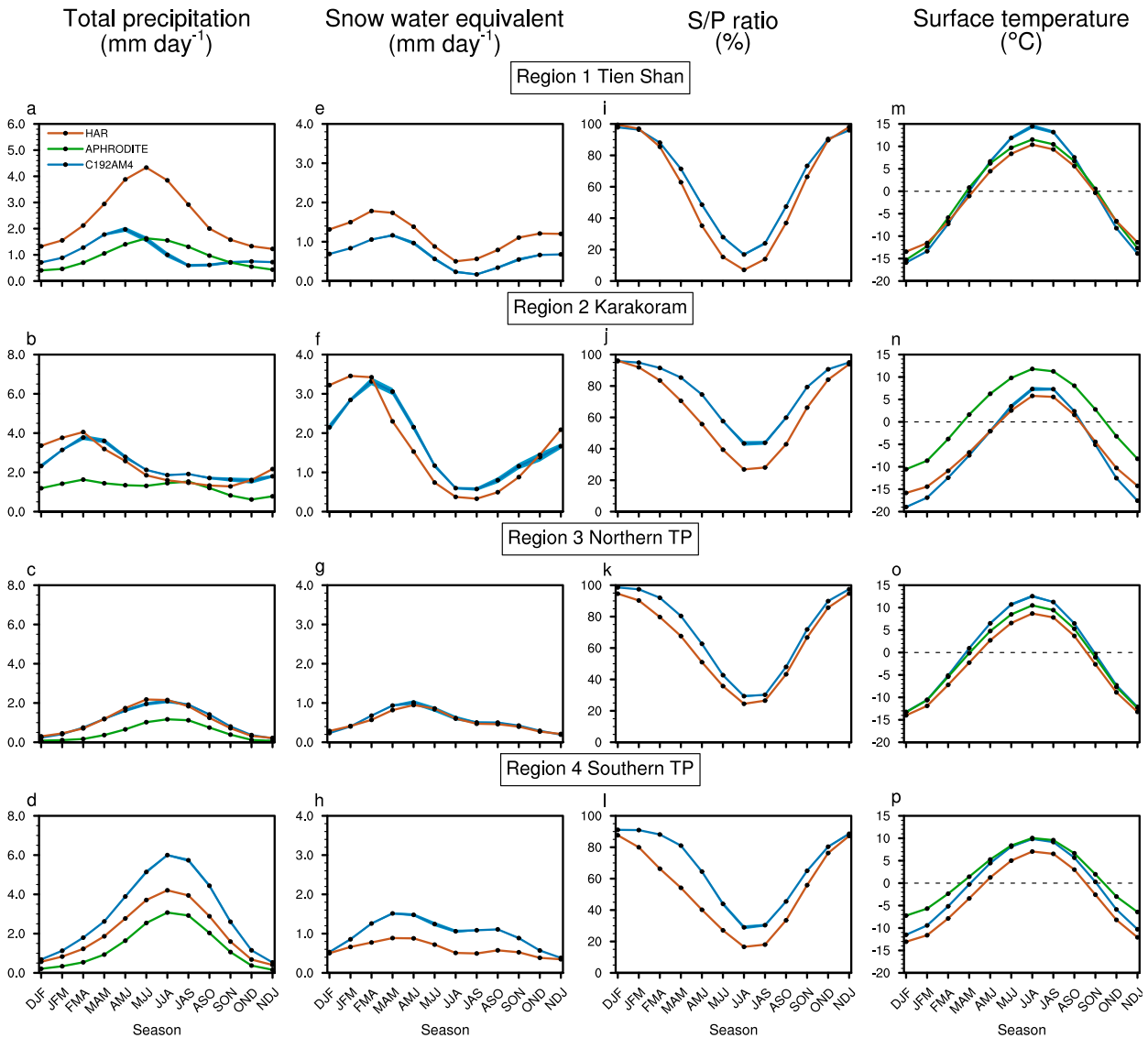
FIG. 3. (a)–(d) Three-month seasonal mean of total precipitation over regions 1 to 4. (e)–(h) As in (a)–(d), but for snow water equivalent. (i)–(l) As in (a)–(d), but for the S/P ratio. (m)–(p) As in (a)–(d), but for surface air temperature. Blue lines show results from the C192AM4 simulations (1950–2014), while brown and green lines show estimates from HAR (2000–14) and APHRODITE (1998–2014). The blue shading indicates the ±1 standard deviation of the three model ensembles. Similar results are obtained if C192AM4 datasets are restricted to the continuous period of 1998–2014.

(Su et al. 2013). The relatively smaller values based on APHRODITE data in all four subregions imply that although the new version product better captures extreme precipitation events, it may not capture the seasonal cycle well in these high-altitude locations when the station density is low. For instance, APHRODITE underestimates the wintertime maximum in total precipitation over the Karakoram region (Fig. 3b). This shortcoming has previously been pointed out by Kapnick et al. (2014) based on in situ observation, who attributed it to the limited coverage of station records in this region. This has been further confirmed by Li et al. (2020) using observation-based gridded data, satellite products, reanalysis data, and regional climate model outputs.

Despite some quantitative differences, the seasonality of snowfall simulated by the C192AM4 agrees well with the HAR product in all four subregions (Figs. 3e–h). As with total precipitation, snowfall is smaller in C192AM4 than in HAR in region 1 and larger in C192AM4 than in HAR in region 4. The wintertime maximum in total precipitation in region 2 can be attributed largely to wintertime snowfall (Fig. 3f). The dominance of wintertime precipitation helps maintain the unique hydroclimate of the Karakoram region (Kapnick et al. 2014; Forsythe et al. 2017). The seasonality of the S/P ratio over all four subregions is characterized by larger values in winter and smaller values in summer (Figs. 3i–l). Also, the mean seasonal cycle is stronger in HAR compared to C192AM4. The
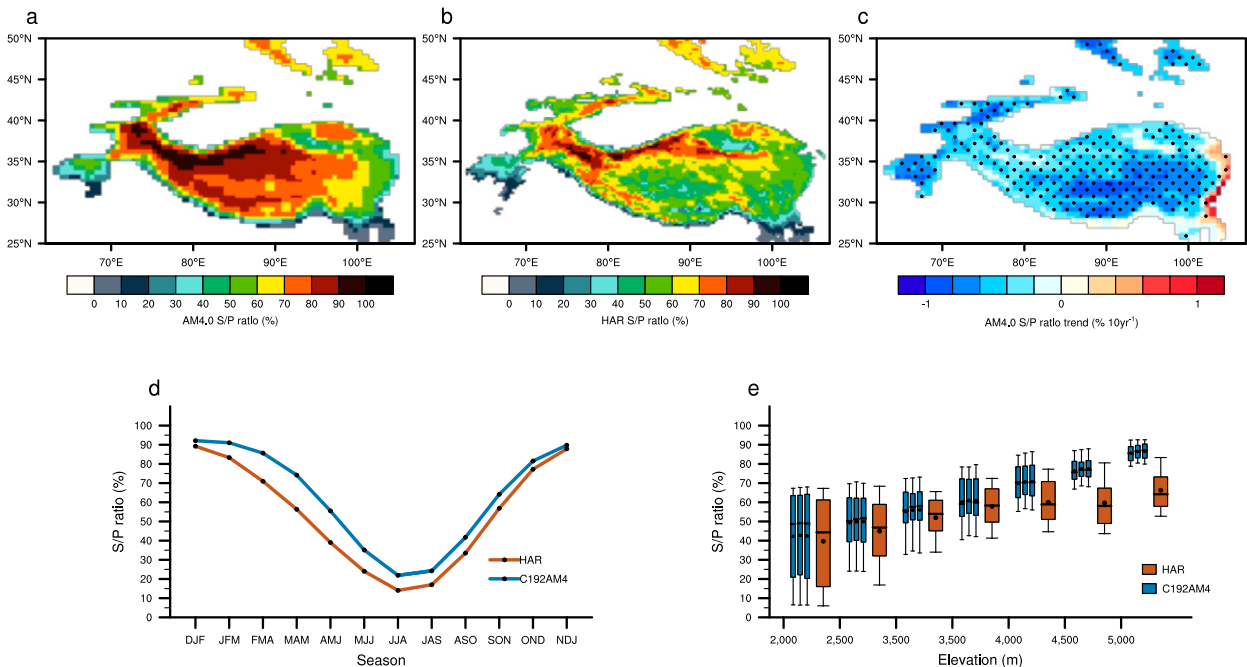
FIG. 4. Long-term mean *S/P* ratios averaged over 2000–14 based on (a) three C192AM4 ensemble members and (b) the HAR dataset over the HMA domain. (c) Linear trends in *S/P* ratios from the C192AM4 simulations for 1950–2014. Dots indicate trends that are statistically significant at the 95% confidence level. (d) Three-month seasonal means of *S/P* ratios averaged over 2000–14 from the three C192AM4 ensemble members (blue) and HAR (brown) over the HMA domain. Blue shading indicates the standard deviation of the three ensembles. (e) Box-and-whisker plot of mean *S/P* ratios binned by elevation into 500-m intervals between 2000 and 5000 m above mean sea level. Boxes indicate the 10th percentile (lower whisker), 25th percentile (lower box edge), median (horizontal line), 75th percentile (upper box edge), and 90th percentile (upper whisker), respectively, as well as the mean (black dot).

large total precipitation in HAR relative to the C192AM4 in region 1 is not mirrored in the *S/P* ratio, indicating that such an overestimation is mainly caused by larger snowfall in HAR. Similarly, the larger total precipitation simulated by C192AM4 in region 4 is also primarily a result of relatively large snowfall in the model. For surface air temperature, elevation errors manifest as a summertime warm bias in C192AM4 relative to HAR (Figs. 3m–p). The greatest difference is found for region 1 (the Tien Shan mountain ranges), where elevation errors are most pronounced as mentioned above (Fig. S1). The APHRODITE dataset also shows a year-round warm bias of approximately 5°C over the Karakoram (region 2) compared to C192AM4 and HAR. This warm bias in temperature helps explain the low bias in total precipitation over the Karakoram in APHRODITE (Fig. 3b). This product is known to underestimate precipitation in regions where frozen precipitation occurs and at high elevations where there are few meteorological stations (Yatagai et al. 2012). Therefore, even if total precipitation is very similar across different products, differences in temperature could affect the partitioning of precipitation into snowfall and rainfall.

c. Characteristics of the S/P ratio

The preceding comparisons demonstrate that, in the absence of continuous observations with broad spatial coverage,

the C192AM4 simulations provide a credible proxy for exploring hydroclimatic variations over HMA. In this section, we explore the characteristics of simulated *S/P* ratios within HMA based mainly on the three-member ensemble of C192AM4 simulations. We also compare the model results with a companion analysis based on HAR data.

The C192AM4 simulations produce broadly similar spatial distributions and seasonal cycles of *S/P* ratios as indicated by HAR (Figs. 4a,b,d). C192AM4 consistently overestimates the mean value by about 10% with respect to the HAR dataset. This overestimation is most pronounced in the interior of Tibetan Plateau, and also increases with increasing surface elevation. Differences in the mean *S/P* ratio are within 5% below the 4000–4500-m interval but rise to more than 15% above this interval (Fig. 4e). Such an overestimation is mainly attributed to the relatively larger portion of snowfall in C192AM4 with respect to the HAR dataset. This is also evident in Fig. 3 (last row) given that grids higher than 4500 m are mainly distributed in region 4. Interestingly, the difference between C192AM4 and HAR is larger in warm seasons, which calls for a close investigation of the partitioning of rain and snow in both models. Figure 4c shows linear trends in *S/P* ratios during the 1950–2014 period as simulated by C192AM4. Significant decreasing trends are simulated across almost all of HMA, with only a small patch of positive trends along the eastern periphery
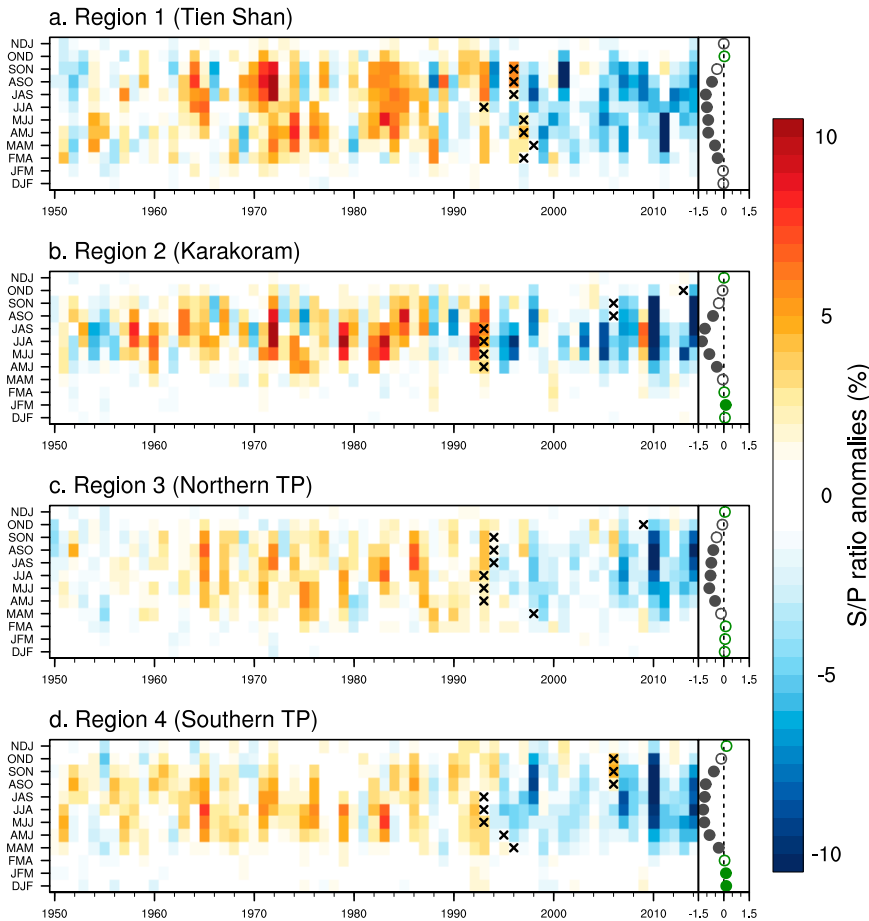
FIG. 5. (a)–(d) Changes in S/P ratio (units: %) by 3-month seasonal mean over regions 1 to 4, respectively, during 1950–2014. Anomalies are calculated relative to the mean for the whole period. Black crosses denote potential regime shifts detected using the changepoint identification algorithm. Linear trends (units: % decade^{-1}) for each season are shown at the rightmost edge of each panel. Solid (open) circles indicate trends that are statistically significant (insignificant) at the 95% confidence level. Positive (negative) trends are circled in green (gray). Seasonal means are calculated for all overlapping periods of three consecutive calendar months.

of the TP. The increasing trend in S/P ratios over the eastern edge of the TP results primarily from the substantial decline in total precipitation shown in Fig. 2d. We return to this topic in the following section.

Figure 5 illustrates how the seasonal cycles of S/P ratios contribute to annual trends across the four subregions. Significant decreasing trends are noted across all subregions during summer months with sporadic and relatively weak positive signals during spring or winter months. Over the Tien Shan mountain range, S/P ratios show decreasing trends year-round with the exception of an insignificant increasing trend centered in November. Changes in S/P ratios are quite similar over the northern and southern portions of the Tibetan Plateau, with decreasing trends during the warm season, and a few weak increasing trends simulated during the cold season from December to March. Compared to the other three regions, the Karakoram region shows a shorter duration of decreasing trends within the annual cycle. Moreover, this region

shows increasing trends in S/P ratios between December and March, during the season when snow constitutes the largest portion of total precipitation. This is consistent with observed increases in glacier mass within the Karakoram region during recent decades (Kapnick et al. 2014; Immerzeel et al. 2015; Forsythe et al. 2017).

As indicated by the shifts from warm to cold colors in Fig. 5, negative anomalies start to emerge around the middle of the 1990s. We apply the climate changepoint detection algorithm to more objectively identify any robust regime shifts in seasonal S/P ratios. This algorithm identifies significant regime shifts around the middle of the 1990s, primarily during the summer months. The timing of the shift in region 1 (1996/97) is about 3 years later than the timing of the shifts in the other three regions (1993/94). More recent regime shifts are also detected in the simulations for some winter months, when the S/P ratio is typically high and the hydroclimate is relatively less sensitive to climate change. This implies that climatic warming
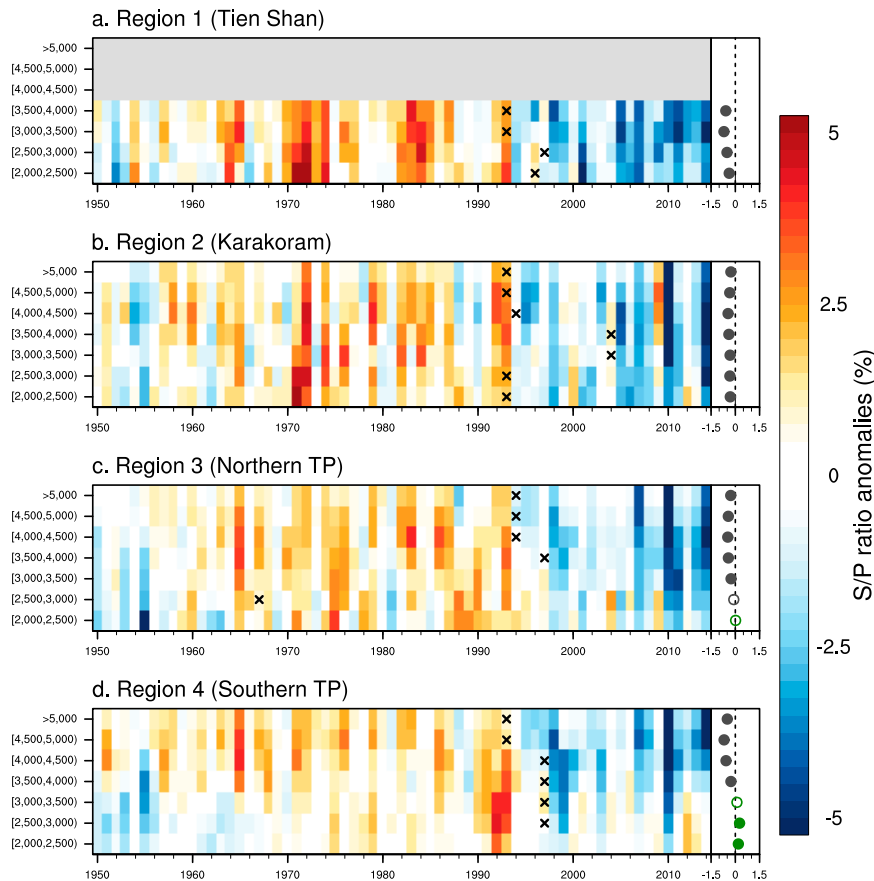
FIG. 6. As in Fig. 5, but for changes in the S/P ratio binned by elevation. Anomalies are calculated on an annual basis in 500-m elevation ranges between 2000 and 5000 m above mean sea level. Gray shading in (a) denotes elevation ranges that are not represented in region 1. Note that the color scale differs from that in Fig. 5.

can exert an effect on these remote mountainous regions even during the cold season, and that the tipping point for such a shift may be imminent if it has not already arrived.

We replicate our analysis using annual mean S/P ratios in 500-m elevation bins to highlight how the annual trends differ as a function of surface elevation in each subregion (Fig. 6). Trends in S/P ratios are uniformly negative and statistically significant across all elevation bins in the Tien Shan and Karakoram regions. However, positive trends are found at low elevations (below 2500 m) in the northern and southern Tibetan Plateau domains. Although insignificant, the positive trend even extends upward into 3000–3500-m bin in the southern Tibetan Plateau. Despite similar elevations, different S/P ratio trends are simulated across the four subregions. The decreasing trend in S/P ratios is smaller in the Karakoram region than in the other three regions at altitudes above 3500 m, which may again help explain the unique Karakoram anomaly. Application of the climate changepoint detection algorithm again identifies transition years around the mid-1990s, as also shown in Fig. 5. Analyses performed on time series of simulated surface air temperature yield similar results (figures not shown). This is consistent with the prior understanding

that the S/P ratio is quite sensitive to changes in temperature (Huntington et al. 2004).

d. Attribution analysis of changes in S/P ratios

The significant decreasing trends in S/P ratios call for careful investigation of the factors that could contribute to these changes. By definition, changes in S/P ratios could result from changes in snowfall, changes in total precipitation, or some combination of the two. Based on Eq. (2), the S/P ratio trend is determined by the relative magnitude of trends in the logarithm of snowfall ($\ln S$) and the logarithm of total precipitation ($\ln P$).

As shown in Fig. 7, we test temporal trends in the logarithms of both total precipitation and snowfall for each month to understand the simulated trends in S/P ratio. For region 1 (Fig. 7a), the trend in total precipitation is weak throughout the year but a strong reduction in snowfall, especially during warm season months, leads to a significant decrease in the S/P ratio. A similar situation is found for the southern Tibetan Plateau, except that reductions in snowfall are statistically ignificant through more of the year (Fig. 7d). For regions 2 and 3, reductions in snowfall are coupled with weak positive trends in total precipitation in several months, amplifying decreases in S/P ratios. We therefore
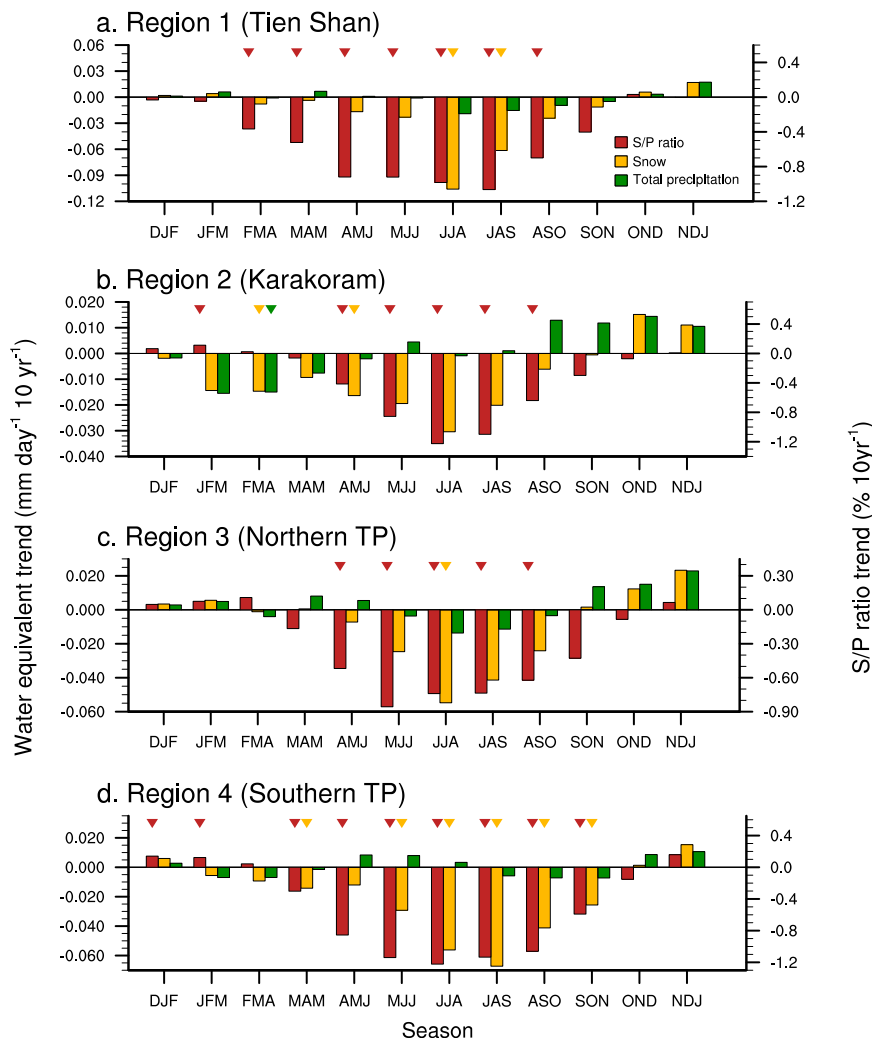
FIG. 7. (a)–(d) Linear trends in snowfall (yellow bars; units: mm day^{-1} 10 yr^{-1}), total precipitation (green bars; units: mm day^{-1} decade^{-1}), and the S/P ratio (red bars; units: % 10 yr^{-1}) by 3-month seasonal mean for regions 1 to 4, respectively. Snowfall and total precipitation are plotted using the left y axis, while the S/P ratio is plotted using the right y axis. Colored triangles indicate linear trends that are statistically significant at the 95% confidence level.

conclude that, throughout the four subregions, decreases in S/P ratios during summertime are dominated by decreases in snowfall amplified in some cases by increases in total precipitation. The latter contribution appears to be more prevalent during the shoulder months (around May and September). Although it does not affect the main conclusion, it is worth noting that the relationship indicated by Eq. (2) is not always satisfied in Fig. 7, especially when the trends are small. This might be related to our use of the Theil–Sen estimator for linear trend calculations, in which trends are estimated as the median slope between all paired values rather than through least squares minimization.

e. Relationships between S/P ratios and surface air temperatures

A decrease in the S/P ratio is a good indicator of a warming climate. To further probe the relationship between the S/P

ratio and surface air temperature in HMA, we apply Eq. (3) to fit the relationships between S/P ratios and surface air temperatures over all four subregions (Fig. 8). Overall, the logistic relationship provides a good fit between these two variables with mean absolute fitting errors (σ) smaller than 0.05 except for southern Tibetan Plateau ($\sigma = 0.06$). During winter months, temperatures are usually well below the freezing point so that small changes in temperature are unlikely to result in large shifts from snowfall to rainfall. As the cold season transitions to the warm season, small changes in temperature can lead to large reductions in the S/P ratio. The scatter points are concentrated along the fitted curve during summer and winter months; however, the points often diverge substantially from the fitted curve during the shoulder months (spring and fall). This divergence from the fitted curve is especially pronounced in region 4. Over this region, the S/P ratio in the fall is about 20% smaller
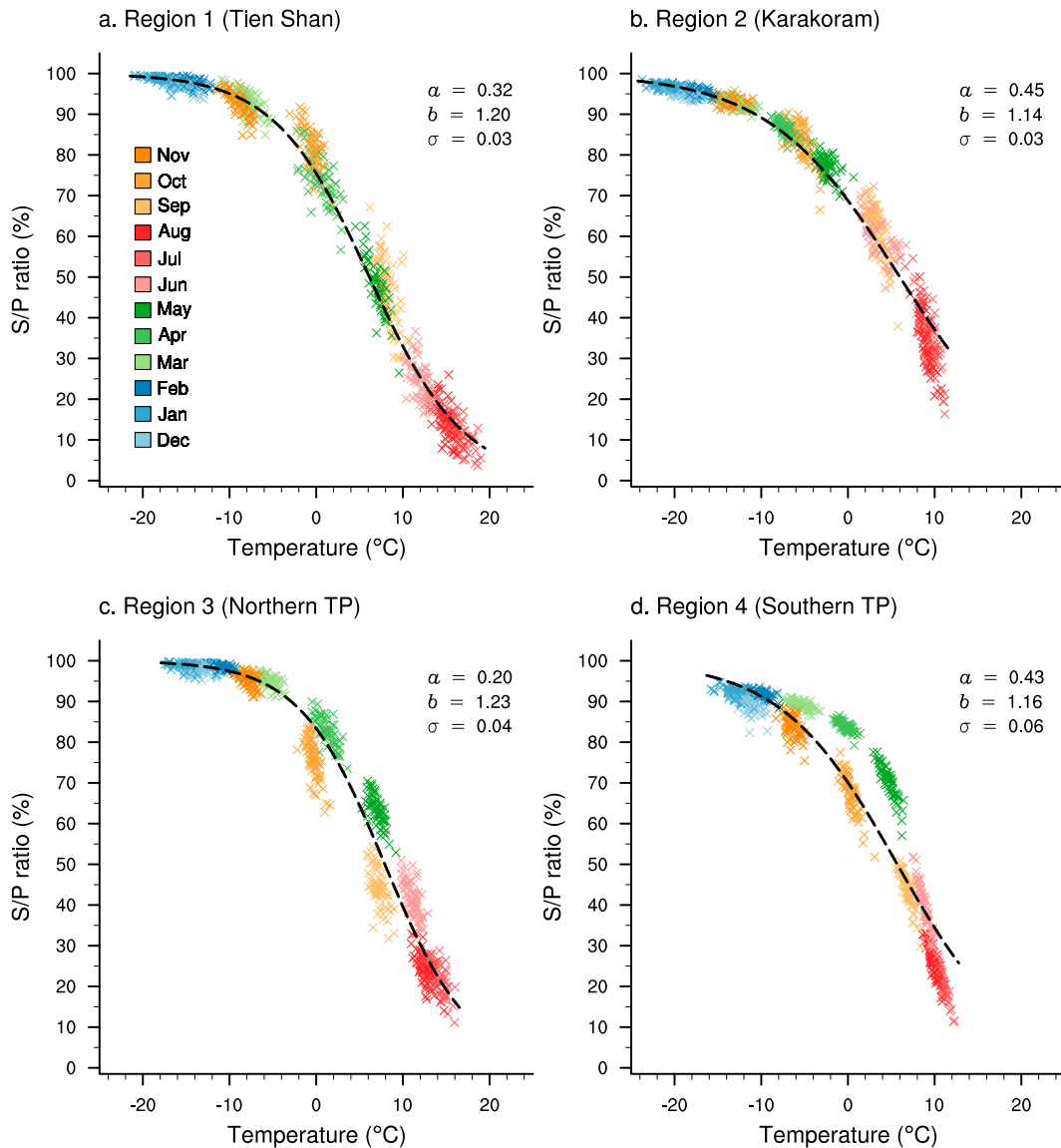
FIG. 8. (a)–(d) Scatterplots of relationships between S/P ratios and surface air temperatures over regions 1 to 4, respectively, during 1950–2014. Each cross represents a pair of monthly mean values as indicated by the colors in the key. Black dashed lines show fits to Eq. (3). The fitting constants a and b and the mean absolute fitting error σ are listed in the upper-right corner of each panel.

than that in the spring given the same value of surface air temperature. This may reflect the lingering influence of the Indian summer monsoon during fall as well as the associated meteorological conditions, and requires further investigation.

Based on the fitting constants, we can calculate the threshold value of surface air temperature for which the expected value of the S/P ratio is equal to 50% ($\overline{T}_{af=0.5}$). This is a useful metric for defining the partitioning of precipitation phase as highlighted by Jennings et al. (2018) and references therein. Precipitation is equally likely to fall as rain or snow at this temperature, while it is primarily in the form of rain for temperatures warmer than this threshold and in the form of snow for temperatures colder than this threshold. On the monthly

scale, the mean temperature thresholds for the four subregions are 6.1°C (region 1), 6.0°C (region 2), 7.9°C (region 3), and 5.7°C (region 4). Our results are consistent with those of Jennings et al. (2018), who suggested that $\overline{T}_{af=0.5}$ is larger than 4.5°C (their Figs. 1 and 3) over HMA based on both precipitation events recorded in station observations at subdaily time scales and their logistic regression model. Our overestimation of $\overline{T}_{af=0.5}$ as derived from the data in Fig. 8 could be related to our use of monthly mean data in this study or the presence of systematic biases toward snowfall in this region based on the C192AM4 model. We have further calculated the fitting constants a and b and the temperature threshold $\overline{T}_{af=0.5}$ for each model grid point (see supplemental Fig. S2). Larger values of
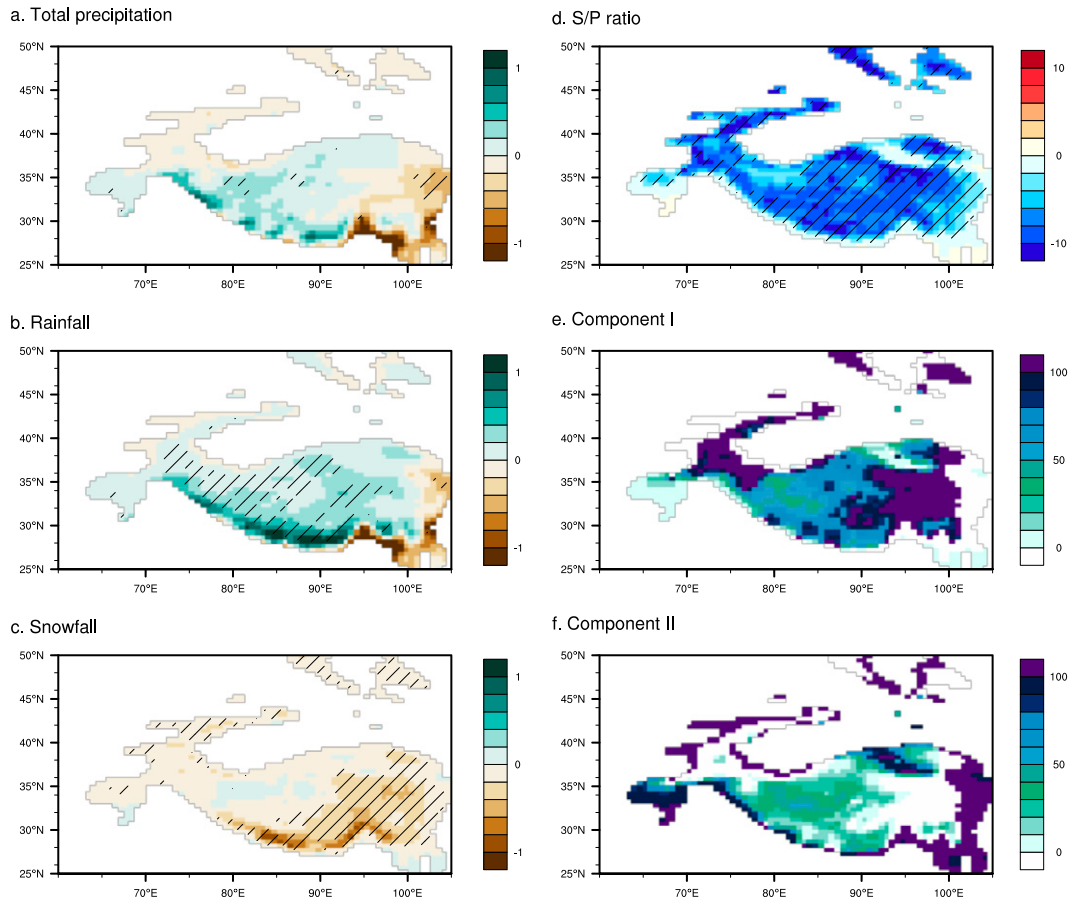
FIG. 9. Difference in (a) total precipitation (mm day^{-1}), (b) rainfall (mm day^{-1}), (c) snowfall (mm day^{-1}), and (d) *S/P* ratio between 2000–14 and 1976–90. (e),(f) Contributions to changes in rainfall (units: %) by the local temperature change component (component I) and the large-scale circulation component (component II). Hatching in (a)–(d) indicates changes that are statistically significant at the 95% confidence level based on the two-tailed Student's *t* test.

the temperature threshold are found at higher elevations, which is consistent with the conclusion of Jennings et al. (2018) that $\overline{T}_{af=0.5}$ is larger at higher elevations in continental regions. But we must take these results with caution: the relationship between the *S/P* ratio and surface temperature could be totally different if higher temporal frequency data are used. Consequently, the value of $\overline{T}_{af=0.5}$ could be substantially different. In fact, despite a similar spatial distribution, the simulated $\overline{T}_{af=0.5}$ is considerably overestimated over HMA compared to the results based on precipitation events at subdaily time scales (Jennings et al. 2018; our supplemental Fig. S2).

f. Attribution analysis of rainfall

The regime shifts in *S/P* ratios identified in section 3c and the attribution analysis in section 3d indicate that C192AM4 simulates increased rainfall over HMA as climate warms. However, it remains unclear whether this increased rainfall should be attributed to changes in temperature (i.e., transformation of snowfall into rainfall associated with the increased

occurrence of temperatures above the freezing point) or changes in the large-scale circulation (i.e., an increase in total precipitation due to increased moisture flux convergence). We explore this question by examining the 15-yr periods before and after the approximate transition year identified using the changepoint algorithm in section 3c. The first period (period I) spans 1976–90 while the second (period II) spans 2000–14. The selection of these two periods is justified that they are in two *S/P* ratio regimes and their differences are robust. The main results change slightly if we use a longer period or switch to another 15-yr period (figures not shown).

We calculate differences in total precipitation, snowfall, rainfall, and *S/P* ratios between these two periods, respectively. As shown in Fig. 9, differences in total precipitation between these two periods are insignificant outside of a few isolated regions. By contrast, simulated rainfall is significantly larger during the second period, while snowfall decreased over almost the entire HMA domain. These changes lead to significant declines in *S/P* ratios. We use Eq. (5) to assess the relative contributions of local temperature changes and total precipitation changes to the rainfall increase. The results

demonstrate that increases in rainfall are primarily from the transformation of snowfall to rainfall over large parts of HMA (component I; Fig. 9e), which is closely related to changes in temperature. Substantial contributions by changes in total precipitation (component II; Fig. 9f) are mainly confined to the peripheral regions of HMA.

4. Conclusions and discussion

In this study, we use the GFDL C192AM4 model to investigate the seasonality and interannual variability of S/P ratios over High Mountain Asia. Comparison with available observations and outputs from a regional model indicates that C192AM4 is able to reliably capture the spatial distributions and seasonal variability of total precipitation, snowfall, and surface air temperature. We identify significant decreasing trends in annual-mean S/P ratios during 1950–2014 along with distinct regime shifts from larger S/P ratios to smaller S/P ratios in the mid-1990s. These tendencies are robust across a range of seasons and elevations, but are most pronounced during the warm season and at higher elevations. Moreover, regime shifts are detected for the winter months during the past decade, suggesting that climatic warming can significantly impact cold season hydroclimate in these remote mountainous regions and may already be doing so. Considering the separate changes in snowfall and total precipitation, decreases in S/P ratios are simulated mainly during the warm season as warming temperatures lead to more precipitation falling in the form of rain rather than snow. Given the distinct effects of snowfall and rainfall on water and energy fluxes at the land surface, we further apply an attribution analysis to distinguish the contributions of local temperature changes relative to those of large-scale dynamics in the transition toward more rainfall-dominated HMA. The results demonstrate that simulated increases in rainfall over recent decades are primarily attributable to the transformation of snowfall to rainfall as temperature warms, although the large-scale dynamical component is more prominent over the peripheral regions of HMA. We further assess links between S/P ratios and surface air temperatures by fitting the model-simulated monthly means to a logistic relationship. This relationship allows for the calculation of the threshold temperature at which the S/P ratio equals 50%, and reveals that this temperature threshold generally increases with increasing elevation.

This study provides an extensive evaluation of changes in S/P ratios over HMA and the mechanisms behind these changes. The results have substantial socioeconomic implications for water management as climate warms. A greater portion of precipitation falling as rainfall could amplify the influence of increased melting rates in intensifying the risk of flooding downstream of the natural reservoirs in HMA. Earlier runoff during springtime will also complicate the management of reservoirs, perhaps requiring summertime water storage for agricultural irrigation to be sacrificed for springtime flood control.

Although many of the key characteristics of precipitation, such as precipitation amount, have been extensively studied under the context of climate change, much less attention has been paid to changes in the phase of precipitation. This study

thus helps complement ongoing research into the hydroclimate of HMA, which remains limited by a lack of reliable long-term observations with adequate spatial coverage. Inaccurate partitioning of precipitation into its liquid and solid phases leads directly to significant biases in key hydrological variables, including soil moisture, snow depth, snow cover, and the timing of spring melt, among others. These biases in turn cause errors in estimates of river runoff, land surface albedo, and land–atmosphere energy exchange. Quantification of changes in S/P ratios relative to their historical values is thus essential for a more accurate and confident assessment of the hydroclimatic response to warming over HMA, both in the present day and in future projections.

Finally, it is worth noting a few caveats of the present study. First, the use of monthly data is not able to represent the variability of precipitation on shorter time scale. Given the irregularity of precipitation events over HMA (Maussion et al. 2014), one should be aware that the relationship between the S/P ratio and surface temperature as well as the temperature threshold could be different if higher-frequency datasets are used. Second, there are large uncertainties in observations over HMA. Although the APHRODITE product makes use of the most available station records, its quality is highly dependent on the amount of input data, which varies largely in space and time over HMA. More accurate observations over the inner and western HMA as well as elevated mountainous areas are needed to provide a coherent picture of changes in the S/P ratio. In addition, the model also has limited ability to simulate convective processes associated with short-duration precipitation events. For example, the model tends to overproduce the mesoscale convective systems (an important rain-bearer over HMA) over southeastern HMA while underestimating them over the Tien Shan (Zhao 2022). This could affect the partitioning between rainfall and snowfall considering that the snowfall in the model is calculated based on an integral measure of lower-tropospheric temperature. The rain–snow partitioning could also be sensitive to the microphysics scheme used in the model as demonstrated by Guo et al. (2021). In this sense, our results would need to be further validated using different models and/or microphysics schemes.

REFERENCES

Bibi, S., L. Wang, X. P. Li, J. Zhou, D. L. Chen, and T. D. Yao, 2018: Climatic and associated cryospheric, biospheric, and hydrological changes on the Tibetan Plateau: A review. *Int. J. Climatol.*, **38**, E1–E17, https://doi.org/10.1002/joc.5411.

Bintanja, R., 2018: The impact of Arctic warming on increased rainfall. *Sci. Rep.*, **8**, 16001, https://doi.org/10.1038/s41598-018-34450-3.

Chen, J., and A. K. Gupta, 2012: *Parametric Statistical Change Point Analysis: With Applications to Genetics, Medicine, and Finance.* Birkhäuser, 273 pp.

Cuo, L., Y. X. Zhang, Q. C. Wang, L. L. Zhang, B. R. Zhou, Z. C. Hao, and F. G. Su, 2013: Climate change on the northern Tibetan Plateau during 1957–2009: Spatial patterns and possible mechanisms. *J. Climate*, **26**, 85–109, https://doi.org/10.1175/JCLI-D-11-00738.1.

Delworth, T. L., and Coauthors, 2012: Simulated climate and climate change in the GFDL CM2.5 high-resolution coupled climate model. *J. Climate*, **25**, 2755–2781, https://doi.org/10.1175/JCLI-D-11-00316.1.

Deng, H. J., N. C. Pepin, and Y. N. Chen, 2017: Changes of snowfall under warming in the Tibetan Plateau. *J. Geophys. Res. Atmos.*, **122**, 7323–7341, https://doi.org/10.1002/2017JD026524.

Ding, Z. Y., R. J. Lu, and Y. Y. Wang, 2019: Spatiotemporal variations in extreme precipitation and their potential driving factors in non-monsoon regions of China during 1961–2017. *Environ. Res. Lett.*, **14**, 024005, https://doi.org/10.1088/1748-9326/aaf2ec.

Dong, W. H., and Coauthors, 2016: Summer rainfall over the southwestern Tibetan Plateau controlled by deep convection over the Indian subcontinent. *Nat. Commun.*, **7**, 10925, https://doi.org/10.1038/ncomms10925.

——, Y. L. Lin, J. S. Wright, Y. Y. Xie, F. H. Xu, W. Q. Xu, and Y. Wang, 2017: Indian monsoon low-pressure systems feed up-and-over moisture transport to the southwestern Tibetan Plateau. *J. Geophys. Res. Atmos.*, **122**, 12 140–12 151, https://doi.org/10.1002/2017JD027296.

——, and Coauthors, 2018a: Regional disparities in warm season rainfall changes over arid eastern-central Asia. *Sci. Rep.*, **8**, 13051, https://doi.org/10.1038/s41598-018-31246-3.

——, and Coauthors, 2018b: Connections between a late summer snowstorm over the southwestern Tibetan Plateau and a concurrent Indian monsoon low-pressure system. *J. Geophys. Res. Atmos.*, **123**, 13 676–13 691, https://doi.org/10.1029/2018JD029710.

——, Y. Ming, and V. Ramaswamy, 2020: Projected changes in South Asian monsoon low pressure systems. *J. Climate*, **33**, 7275–7287, https://doi.org/10.1175/JCLI-D-20-0168.1.

——, M. Zhao, Y. Ming, and V. Ramaswamy, 2021: Representation of tropical mesoscale convective systems in a general circulation model: Climatology and response to global warming. *J. Climate*, **34**, 5657–5671, https://doi.org/10.1175/JCLI-D-20-0535.1.

Dunne, J. P., and Coauthors, 2020: The GFDL Earth system model version 4.1 (GFDL-ESM 4.1): Overall coupled model description and simulation characteristics, **12**, e2019MS002015, https://doi.org/10.1029/2019MS002015.

Eyring, V., S. Bony, G. A. Meehl, C. A. Senior, B. Stevens, R. J. Stouffer, and K. E. Taylor, 2016: Overview of the Coupled Model Intercomparison Project Phase 6 (CMIP6) experimental design and organization. *Geosci. Model Dev.*, **9**, 1937–1958, https://doi.org/10.5194/gmd-9-1937-2016.

Feng, S., and Q. Hu, 2007: Changes in winter snowfall/precipitation ratio in the contiguous United States. *J. Geophys. Res.*, **112**, D15109, https://doi.org/10.1029/2007JD008397.

Førland, E. J., and I. Hanssen-Bauer, 2000: Increased precipitation in the Norwegian Arctic: True or false? *Climatic Change*, **46**, 485–509, https://doi.org/10.1023/A:1005613304674.

Forsythe, N., H. J. Fowler, X. F. Li, S. Blenkinsop, and D. Pritchard, 2017: Karakoram temperature and glacial melt driven by regional atmospheric circulation variability. *Nat. Climate Change*, **7**, 664–670, https://doi.org/10.1038/nclimate3361.

Guo, H., Y. Ming, S. Fan, L. Zhou, L. Harris, and M. Zhao, 2021: Two-moment bulk cloud microphysics with prognostic precipitation in GFDL's Atmosphere Model AM4.0: Configuration and performance. *J. Adv. Model. Earth Syst.*, **13**, e2020MS002453, https://doi.org/10.1029/2020MS002453.

Guo, L. P., and L. H. Li, 2015: Variation of the proportion of precipitation occurring as snow in the Tian Shan Mountains, China. *Int. J. Climatol.*, **35**, 1379–1393, https://doi.org/10.1002/joc.4063.

Harpold, A. A., and Coauthors, 2017: Rain or snow: Hydrologic processes, observations, prediction, and research needs. *Hydrol. Earth Syst. Sci.*, **21**, 1–22, https://doi.org/10.5194/hess-21-1-2017.

Held, I. M., and Coauthors, 2019: Structure and performance of GFDL's CM4.0 climate model. *J. Adv. Model. Earth Syst.*, **11**, 3691–3727, https://doi.org/10.1029/2019MS001829.

Huntington, T. G., G. A. Hodgkins, B. D. Keim, and R. W. Dudley, 2004: Changes in the proportion of precipitation occurring as snow in New England (1949–2000). *J. Climate*, **17**, 2626–2636, https://doi.org/10.1175/1520-0442(2004)017<2626:CITPOP>2.0.CO;2.

Ikeda, K., and Coauthors, 2010: Simulation of seasonal snowfall over Colorado. *Atmos. Res.*, **97**, 462–477, https://doi.org/10.1016/j.atmosres.2010.04.010.

Immerzeel, W. W., N. Wanders, A. F. Lutz, J. M. Shea, and M. F. P. Bierkens, 2015: Reconciling high-altitude precipitation in the upper Indus basin with glacier mass balances and runoff. *Hydrol. Earth Syst. Sci.*, **19**, 4673–4687, https://doi.org/10.5194/hess-19-4673-2015.

IPCC, 2019: High mountain areas. *The Ocean and Cryosphere in a Changing Climate.* Cambridge University Press, 131–202.

Jennings, K. S., T. S. Winchell, B. Livneh, and N. P. Molotch, 2018: Spatial variation of the rain–snow temperature threshold across the Northern Hemisphere. *Nat. Commun.*, **9**, 1148, https://doi.org/10.1038/s41467-018-03629-7.

Kapnick, S. B., T. L. Delworth, M. Ashfaq, S. Malyshev, and P. C. D. Milly, 2014: Snowfall less sensitive to warming in Karakoram than in Himalayas due to a unique seasonal cycle. *Nat. Geosci.*, **7**, 834–840, https://doi.org/10.1038/ngeo2269.

Knowles, N., M. D. Dettinger, and D. R. Cayan, 2006: Trends in snowfall versus rainfall in the western United States. *J. Climate*, **19**, 4545–4559, https://doi.org/10.1175/JCLI3850.1.

Krasting, J. P., A. J. Broccoli, K. W. Dixon, and J. R. Lanzante, 2013: Future changes in Northern Hemisphere snowfall. *J. Climate*, **26**, 7813–7828, https://doi.org/10.1175/JCLI-D-12-00832.1.

Legates, D. R., and T. A. Bogart, 2009: Estimating the proportion of monthly precipitation that falls in solid form. *J. Hydrometeor.*, **10**, 1299–1306, https://doi.org/10.1175/2009JHM1086.1.

Levine, X. J., and W. R. Boos, 2017: Land surface albedo bias in climate models and its association with tropical rainfall. *Geophys. Res. Lett.*, **44**, 6363–6372, https://doi.org/10.1002/2017GL072510.

Li, D., K. Yang, W. Tang, X. Li, X. Zhou, and D. Guo, 2020: Characterizing precipitation in high altitudes of the western Tibetan Plateau with a focus on major glacier areas. *Int. J. Climatol.*, **40**, 5114–5127, https://doi.org/10.1002/joc.6509.

Li, Q., T. Yang, Z. M. Qi, and L. H. Li, 2018: Spatiotemporal variation of snowfall to precipitation ratio and its implication on water resources by a regional climate model over Xinjiang, China. *Water*, **10**, 1463, https://doi.org/10.3390/w10101463.

Lin, C., D. Chen, K. Yang, and T. Ou, 2018: Impact of model resolution on simulating the water vapor transport through the central Himalayas: Implication for models' wet bias over the Tibetan Plateau. *Climate Dyn.*, **51**, 3195–3207, https://doi.org/10.1007/s00382-018-4074-x.

Liu, X. D., and B. D. Chen, 2000: Climatic warming in the Tibetan Plateau during recent decades. *Int. J. Climatol.*, **20**, 1729–1742, https://doi.org/10.1002/1097-0088(20001130)20:14<1729::AID-JOC556>3.0.CO;2-Y.

Lutz, A. F., W. W. Immerzeel, A. B. Shrestha, and M. F. P. Bierkens, 2014: Consistent increase in High Asia's runoff due to increasing glacier melt and precipitation. *Nat. Climate Change*, **4**, 587–592, https://doi.org/10.1038/nclimate2237.

Ma, Y. M., and Coauthors, 2017: Monitoring and modeling the Tibetan Plateau's climate system and its impact on East Asia. *Sci. Rep.*, **7**, 44574, https://doi.org/10.1038/srep44574.

Maussion, F., D. Scherer, T. Mölg, E. Collier, J. Curio, and R. Finkelnburg, 2014: Precipitation seasonality and variability over the Tibetan Plateau as resolved by the High Asia reanalysis. *J. Climate*, **27**, 1910–1927, https://doi.org/10.1175/JCLI-D-13-00282.1.

Mölg, T., and D. Scherer, 2012: Retrieving important mass-balance model parameters from AWS measurements and high-resolution mesoscale atmospheric modeling. *J. Glaciol.*, **58**, 625–628, https://doi.org/10.3189/2012JoG11J258.

——, F. Maussion, and D. Scherer, 2014: Mid-latitude westerlies as a driver of glacier variability in monsoonal High Asia. *Nat. Climate Change*, **4**, 68–73, https://doi.org/10.1038/nclimate2055.

Pepin, N., and Coauthors, 2015: Elevation-dependent warming in mountain regions of the world. *Nat. Climate Change*, **5**, 424–430, https://doi.org/10.1038/nclimate2563.

Raup, B., A. Racoviteanu, S. J. S. Khalsa, C. Helm, R. Armstrong, and Y. Arnaud, 2007: The GLIMS geospatial glacier database: A new tool for studying glacier change. *Global Planet. Change*, **56**, 101–110, https://doi.org/10.1016/j.gloplacha.2006.07.018.

Rawlins, M. A., C. J. Willmott, A. Shiklomanov, E. Linder, S. Frolking, R. B. Lammers, and C. J. Vorosmarty, 2006: Evaluation of trends in derived snowfall and rainfall across Eurasia and linkages with discharge to the Arctic Ocean. *Geophys. Res. Lett.*, **33**, L07403, https://doi.org/10.1029/2005GL025231.

Sen, P. K., 1968: Estimates of the regression coefficient based on Kendall's tau. *J. Amer. Stat. Assoc.*, **63**, 1379–1389, https://doi.org/10.1080/01621459.1968.10480934.

Song, M. H., Y. M. Ma, Y. Zhang, M. S. Li, W. Q. Ma, and F. L. Sun, 2011: Climate change features along the Brahmaputra Valley in the past 26 years and possible causes. *Climatic Change*, **106**, 649–660, https://doi.org/10.1007/s10584-010-9950-2.

Su, F. G., X. L. Duan, D. L. Chen, Z. C. Hao, and L. Cuo, 2013: Evaluation of the global climate models in the CMIP5 over the Tibetan Plateau. *J. Climate*, **26**, 3187–3208, https://doi.org/10.1175/JCLI-D-12-00321.1.

Theil, H., 1950: A rank-invariant method of linear and polynomial regression analysis I. *Nederl. Akad. Wetensch. Proc.*, **53**, 386–392.

Tian, H. Z., T. B. Yang, and Q. P. Liu, 2014: Climate change and glacier area shrinkage in the Qilian mountains, China, from 1956 to 2010. *Ann. Glaciol.*, **55**, 187–197, https://doi.org/10.3189/2014AoG66A045.

Tian, L. D., T. D. Yao, A. Numaguti, and W. Z. Sun, 2001: Stable isotope variations in monsoon precipitation on the Tibetan Plateau. *J. Meteor. Soc. Japan*, **79**, 959–966, https://doi.org/10.2151/jmsj.79.959.

Wang, B., Q. Bao, B. Hoskins, G. Wu, and Y. Liu, 2008: Tibetan Plateau warming and precipitation change in East Asia. *Geophys. Res. Lett.*, **35**, L14702, https://doi.org/10.1029/2008GL034330.

Wang, J., M. J. Zhang, S. J. Wang, Z. G. Ren, Y. J. Che, F. Qiang, and D. Y. Qu, 2016: Decrease in snowfall/rainfall ratio in the Tibetan Plateau from 1961 to 2013. *J. Geogr. Sci.*, **26**, 1277–1288, https://doi.org/10.1007/s11442-016-1326-8.

Wang, N. N., and J. C. Yin, 2019: Self-organizing map network-based precipitation regionalization for the Tibetan Plateau and regional precipitation variability. *Theor. Appl. Climatol.*, **135**, 29–44, https://doi.org/10.1007/s00704-017-2349-5.

Wang, X. J., G. J. Pang, and M. X. Yang, 2018: Precipitation over the Tibetan Plateau during recent decades: A review based on observations and simulations. *Int. J. Climatol.*, **38**, 1116–1131, https://doi.org/10.1002/joc.5246.

Xu, X. D., C. G. Lu, X. H. Shi, and S. T. Gao, 2008: World water tower: An atmospheric perspective. *Geophys. Res. Lett.*, **35**, L20815, https://doi.org/10.1029/2008GL035867.

Yang, K., B. S. Ye, D. G. Zhou, B. Y. Wu, T. Foken, J. Qin, and Z. Y. Zhou, 2011: Response of hydrological cycle to recent climate changes in the Tibetan Plateau. *Climatic Change*, **109**, 517–534, https://doi.org/10.1007/s10584-011-0099-4.

——, H. Wu, J. Qin, C. G. Lin, W. J. Tang, and Y. Y. Chen, 2014: Recent climate changes over the Tibetan Plateau and their impacts on energy and water cycle: A review. *Global Planet. Change*, **112**, 79–91, https://doi.org/10.1016/j.gloplacha.2013.12.001.

Yao, T. D., X. D. Liu, N. L. Wang, and Y. F. Shi, 2000: Amplitude of climatic changes in Qinghai-Tibetan Plateau. *Chin. Sci. Bull.*, **45**, 1236–1243, https://doi.org/10.1007/BF02886087.

——, and Coauthors, 2012: Different glacier status with atmospheric circulations in Tibetan Plateau and surroundings. *Nat. Climate Change*, **2**, 663–667, https://doi.org/10.1038/nclimate1580.

Yatagai, A., K. Kamiguchi, O. Arakawa, A. Hamada, N. Yasutomi, and A. Kitoh, 2012: APHRODITE constructing a long-term daily gridded precipitation dataset for Asia based on a dense network of rain gauges. *Bull. Amer. Meteor. Soc.*, **93**, 1401–1415, https://doi.org/10.1175/BAMS-D-11-00122.1.

Zhang, C., Q. H. Tang, D. L. Chen, R. J. van der Ent, X. C. Liu, W. H. Li, and G. G. Haile, 2019: Moisture source changes contributed to different precipitation changes over the northern and southern Tibetan Plateau. *J. Hydrometeor.*, **20**, 217–229, https://doi.org/10.1175/JHM-D-18-0094.1.

Zhao, M., 2020: Simulations of atmospheric rivers, their variability, and response to global warming using GFDL's new high-resolution general circulation model. *J. Climate*, **33**, 10287–10303, https://doi.org/10.1175/JCLI-D-20-0241.1.

——, 2022: A study of AR-, TS-, and MCS-associated precipitation and extreme precipitation in present and warmer climates. *J. Climate*, **35**, 479–497, https://doi.org/10.1175/JCLI-D-21-0145.1.

——, and Coauthors, 2018a: The GFDL Global Atmosphere and Land Model AM4.0/LM4.0:1. Simulation characteristics with prescribed SSTs. *J. Adv. Model. Earth Syst.*, **10**, 691–734, https://doi.org/10.1002/2017MS001208.

——, and Coauthors, 2018b: The GFDL Global Atmosphere and Land Model AM4.0/LM4.0:2. Model description, sensitivity studies, and tuning strategies. *J. Adv. Model. Earth Syst.*, **10**, 735–769, https://doi.org/10.1002/2017MS001209.

Zhu, X. F., and Coauthors, 2017: Characteristics of the ratios of snow, rain and sleet to precipitation on the Qinghai-Tibet Plateau during 1961–2014. *Quat. Int.*, **444**, 137–150, https://doi.org/10.1016/j.quaint.2016.07.030.